The native material limit of electron and hole mobilities in semiconductor nanowires

Jörg B. Kinzel, Florian J. R. Schülein, Matthias Weiß, Lisa Janker, Dominik D. Bühler, Michael Heigl, Daniel Rudolph, Stefanie Morkötter, Markus Döblinger, Max Bichler, Gerhard Abstreiter, Jonathan J. Finley, Achim Wixforth, Gregor Koblmüller, Hubert J. Krenner

Angaben zur Veröffentlichung / Publication details:

Kinzel, Jörg B., Florian J. R. Schülein, Matthias Weiß, Lisa Janker, Dominik D. Bühler, Michael Heigl, Daniel Rudolph, et al. 2016. "The native material limit of electron and hole mobilities in semiconductor nanowires." *ACS Nano* 10 (5): 4942–53. https://doi.org/10.1021/acsnano.5b07639.

ACSNANO www.acsnano.org

ARTICLE

The Native Material Limit of Electron and Hole Mobilities in Semiconductor Nanowires

Jörg B. Kinzel,[†,‡] Florian J. R. Schülein,[†,‡] Matthias Weiß,[†,‡] Lisa Janker,[†,‡] Dominik D. Bühler,[†] Michael Heigl,[†] Daniel Rudolph,[§,‡] Stefanie Morkötter,[§,‡] Markus Döblinger,[∥,⊥] Max Bichler,[§] Gerhard Abstreiter,[§,#,‡] Jonathan J. Finley,[§,‡] Achim Wixforth,[†,‡,⊥] Gregor Koblmüller,[§,‡] and Hubert J. Krenner*[,†,‡,⊥]

[†]Lehrstuhl für Experimentalphysik 1 and Augsburg Centre for Innovative Technologies (ACIT), Universität Augsburg, Universitätsstraße 1, 86159 Augsburg, Germany

[‡]Nanosystems Initiative Munich (NIM), Schellingstraße 4, 80339 München, Germany

[§]Walter Schottky Institut and Physik Department E24, Technische Universität München, Am Coulombwall 4, 85748 Garching, Germany

[∥]Department of Chemistry, Ludwig-Maximilians-Universität München, 81377 München, Germany

[⊥]Center for Nanoscience (CeNS), Ludwig-Maximilians-Universität München, Geschwister-Scholl-Platz 1, 80539 München, Germany

[#]Institute for Advanced Study (IAS), Technische Universität München, Lichtenbergstraße 2a, 85748 Garching, Germany

ABSTRACT: **Piezoelectric surface acoustic waves are employed to induce radio frequency spatiotemporal dynamics of photogenerated electrons and holes in the GaAs core of individual GaAs/AlGaAs core/shell semiconductor nanowires. Comparison of the time-dependent interband optical recombination to numerical simulations allow to determine the charge carrier transport mobilities of electrons, $\mu_e = 500^{+500}_{-250}$ cm^2/(V s), holes, $\mu_h = 50^{+50}_{-30}$ cm^2/(V s) and their ratio μ_e:μ_h = (20 ± 5):1. Our method probes carrier transport at low carrier density. Thus, the obtained values represent the native material limit of these nanowires, determined by their structural properties. We show that for near-pristine nanowires, individual twin defects do not significantly affect electrical transport, in strong contrast to polytypic nanowires. In the acoustoelectrically modulated emission, we observe unambiguous signatures of (i) hole localization within long wurtzite-rich segments and (ii) electrons in zinc blende regions being reflected at the interface to a wurtzite-rich region. The experimentally observed periodic emission bursts are faithfully reproduced by advanced numerical simulations which include static band edge discontinuities between a single wurtzite segment in an otherwise pure zinc blende nanowire. Otherwise using the same input parameters as for near-pristine zinc blende nanowires, we can deduce from our simulations a minimum conduction band offset of $\Delta E_C \approx 20$ meV at the interface between the zinc blende part and the wurtzite-rich region. These results furthermore confirm that a single wurtzite segment with sufficiently large band offsets efficiently traps holes and blocks electron transport.**

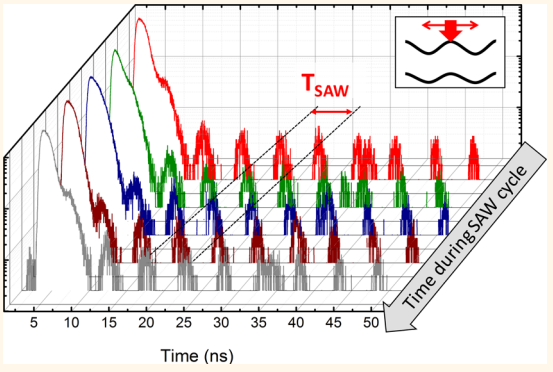

KEYWORDS: *surface acoustic waves, acoustic charge transport, nanowires, polytypism, charge carrier mobility*

Surface acoustic waves (SAWs) have been employed as a versatile conductivity probe in bulk and nanoscale semiconductor structures at radio frequencies (RF) employing the acoustoelectric coupling between charge carriers and the SAW's piezoelectric field.[1−9] SAW-spectroscopy is in particular sensitive in the limit of low carrier concentrations and low conductivities and, in strong contrast to all-electrical approaches, does not require any direct electrical contacts. In this conventional SAW-spectroscopy, the conductivity is derived from the attenuation of the SAW by shunt currents of the mobile carriers. Thus, its sensitivity can decrease significantly for small submicron objects, for instance semiconductor nanowires (NWs). For optically active semiconductors, this limitation can be however appropriately overcome: in these materials the large electric fields accompanying the SAW even efficiently dissociate photogenerated electron−hole pairs (excitons), thus suppressing their radiative recombination.[10−13] The underlying spatiotem-

Received: December 4, 2015
Accepted: March 23, 2016
Published: March 23, 2016

DOI: 10.1021/acsnano.5b07639
ACS Nano 2016, 10, 4942−4953

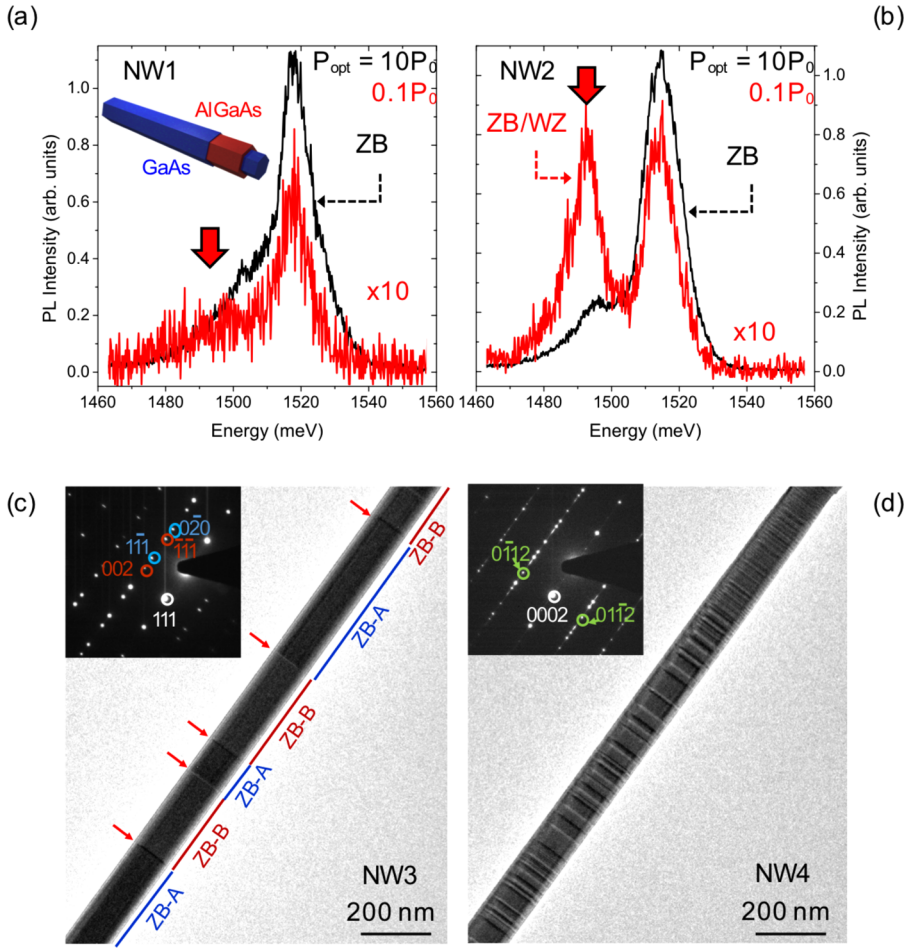

Figure 1. (a,b) Optical emission spectra GaAs/AlGaAs core/shell NWs (inset). Normalized emission spectra of near-pristine NW1 (a) and polytypic NW2 (b) at low (red) and moderate (black) optical pump power. The red-shifted PL emission characteristic for WZ segments in ZB NWs (red arrow) is clearly observed for NW2 but almost completely absent for NW1. (c,d) TEM micrographs and corresponding diffraction patterns (inset) of two representative types of NWs; (c) near-pristine NW3 with ZB phase and only very few twin defects (marked by red arrows) separating individual ZB domains denoted as ZB-A, ZB-B. (d) NW4 with high-density of defects including WZ-phase inclusions, as also marked by WZ-sensitive reflections ($0\bar{1}12$) and ($01\bar{1}2$). These reflections are absent for near pristine NW3.

poral carrier dynamics (STCDs) induced by the SAW can be modeled with high fidelity. Moreover, the experimental signal, temporal modulation of the optical (photoluminescence, PL) emission, can be derived from such calculated electron and hole trajectories.[14,15] The such dissociated electrons and holes are stored and transported over macroscopic distances by the SAW and injected into quantum dots for precisely triggered single photon emission.[16−19] Very recently, first SAW experiments have been performed on individual semiconductor nanowires (NW) and heterostructure NWs transferred on highly piezoelectric $LiNbO_3$ SAW chips and exciton dissociation, carrier transport and injection have been successfully established.[20−24] However, no detailed and complete studies on the SAW-induced STCDs have been reported. As these STCDs depend mainly on the transport mobility of the involved electrons and holes, combined SAW-based acousto-optoelectric spectroscopy provides a direct route to determine these key figures of merit. The transport mobilities of *both* carrier species can be deduced from a direct comparison between the experimentally observed and calculated electron−hole interband recombination. The employed optical spectroscopy is routinely performed on individual, not intentionally doped NWs at the diffraction limit and weak optical pumping. Thus, acousto-optoelectric spectroscopy is in fact ideally suited to determine transport mobilities of *both* carrier species in the native material limit of vanishing carrier density and study the impact of local potential modulations. So far, comparative studies of these key figures of merits on individual NWs have not been reported. In semiconductor NWs nanoscopic mixing of different zinc blende (ZB) and wurtzite (WZ) crystal phases along the NWs axis is frequently observed.[25−31] This polytypism leads to a static modulation of the conduction (CB) and valence band (VB) edges. So far, carrier localization within these potential modulations has been resolved in optical emission spectra;[32−37] however, there exist only a few studies on the impact of these potential barriers on the electrical charge transport.[38,39] As polytypism is absent for bulk crystals, NWs uniquely enable fundamental studies of its impact on carrier transport and SAW-driven STCDs.

Here we report on acousto-optoelectric experiments performed on single GaAs/$Al_{0.3}Ga_{0.7}As$ (GaAs/AlGaAs) core/shell NWs in which we dynamically induce carrier motion along the NW axis using a piezoelectric SAW. We resolve the resulting SAW-driven STCDs in the temporal modulation of the NW's optical *interband* emission. We show that for near-pristine NWs carrier dynamics set in for weak electric fields and

DOI: 10.1021/acsnano.5b07639
ACS Nano 2016, 10, 4942−4953

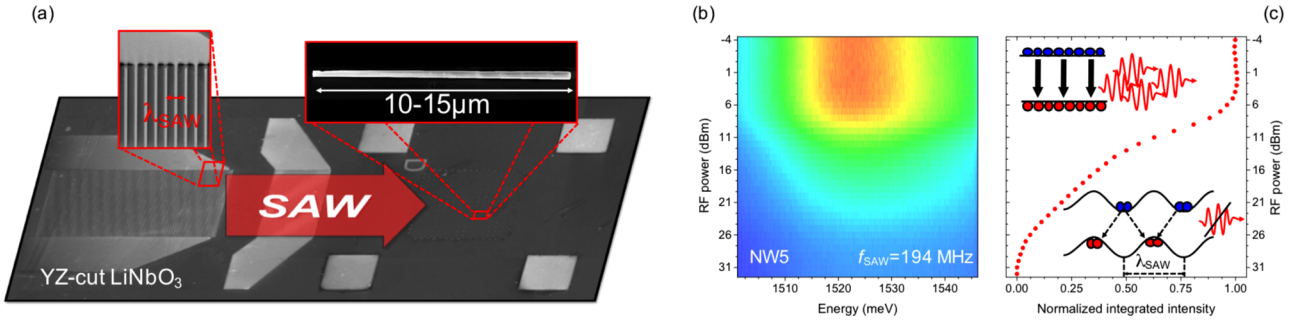

Figure 2. (a) SEM image of typical SAW chip for single NW acoustoelectric spectroscopy. Magnified image shows the finger structure of an IDT used for SAW generation and a single NW aligned with the SAW's propagation direction. (b,c) Color-coded PL-emission of near-pristine NW5 as a function of photon energy and levels P_{RF} (b) and extracted integrated and normalized PL intensity as a function of P_{RF} (c). The observed clear suppression as P_{RF} increases arises from exciton dissociation in the SAW-induced type-II band edge modulation (inset).

that these carrier dynamics are not affected by low density twin boundaries. This is in strong contrast to polytypic NWs: we find that weak polytypism and the resulting segmentation in ZB and WZ regions initially inhibits the carrier flow. Low mobility holes are initially trapped within WZ regions. As the SAW amplitude and thus electric field increase the initially localized carriers overcome potential barriers and transport sets in. Comparing our experimental data to numerical solutions of the SAW-driven carrier dynamics we derive the transport mobilities *of both carrier species* in the native material limit of vanishing carrier density.

RESULTS AND DISCUSSION

We start by comparing PL emission spectra of individual GaAs/AlGaAs core/shell NWs. Details on the growth and layer sequence are summarized in the Methods section. In Figure 1(a) and (b) we present PL spectra of two representative NWs, labeled NW1 and NW2 at low (red) and moderate (black) optical pumping intensity at a temperature of T = 10 K. While for NW1 only the characteristic ZB emission signal is detected at photon energy E_{ZB} = 1518 meV in both spectra, the PL of NW2 shows a characteristic double peak under weak optical pumping ($0.1P_0$ = 500 nW, red). In addition to the ZB emission, which is also the dominant signal under moderate optical pumping ($10P_0$), pronounced PL is detected at lower energy at $E_{ZB/WZ}$ = 1490 meV under weak optical pumping marked by a red arrow. This additional signal is well understood to stem from spatially indirect electron−hole recombination with the electron and hole being localized in ZB and WZ segments, respectively. As this signal is absent for NW1 and only present at low optical pump intensities for NW2, we can conclude that NW1 exhibits a low degree of polytypism, while for NW2 the mixing between the two crystal phases is more pronounced. NW1 exhibits an exponential decay of the PL emission with a time constant $\tau_{PL}^{(NW1)}$ = 1.6 ns, while the decay of NW2 shows the expected biexponential transient[40] with fast and slow time constants of $\tau_{PL,1}^{(NW2)}$ = 1.1 ns and $\tau_{PL,2}^{(NW2)}$ = 8.4 ns, respectively [*cf.* red transients in Figures 2(a,b) and 6(a)]. These long decay times confirm the efficient suppression of nonradiative surface recombination and spatial confinement of carriers to the NW core.[41] We performed transmission electron microscopy (TEM) on representative NWs from this growth run to support our optical data analysis. For NW3 shown in Figure 1(c), we resolve >50 nm long ZB domains, labeled ZB-A (blue) and ZB-B (red), which are separated by individual twin defects. The diffraction pattern (inset) exhibits exclusively characteristic ZB reflections for both types of segments (marked by red and blue circles). On the other hand, the TEM of NW4 shown in Figure 1(d) consists of both ZB and WZ segments. As a consequence, we identify the corresponding characteristic WZ reflections (marked by green and white circles) in the diffraction pattern (inset). Taken together, our optical and structural investigations clearly support the presence of two families of NWs: near-pristine NWs (NW1 and NW3) of ZB phase with a low twin defect density, and polytypic NWs (NW2 and NW4) with WZ segments embedded in an otherwise ZB phase NW.

All optical experiments were performed on NWs transferred onto a highly piezoelectric YZ-cut $LiNbO_3$ substrate.[20,21,24] These substrates were patterned with interdigital transducers (IDTs) as described in the Methods section to facilitate SAW excitation.[42] A scanning electron micrograph (SEM) of a typical SAW-chip for single NW acousto-optoelectric spectroscopy with a magnified image to the IDT fingers and a single NW is shown in Figure 2(a). The larger of the two transducers on the left was used in our experiments to excite a SAW with a wavelength of λ_{SAW} = 18 μm. The length of the NWs ranges between 10 and 15 μm corresponding to approximately 50−80% of the acoustic wavelength. This SAW propagates at the phase velocity of the $LiNbO_3$ substrate of c_s = 3.5 μm/ns. λ_{SAW} converts to a frequency and period of f_{SAW} = 194 MHz and T_{SAW} = 5.1 ns, respectively. In Figure 2(b), the time-integrated PL emission of a single near-pristine NW5 with similar optical properties as NW1 is spectrally analyzed for different RF power levels (P_{RF}) applied to the IDT. The detected PL intensity (normalized to the maximum at low P_{RF} < 4 dBm) is plotted in color scale as a function of P_{RF} and photon energy. The normalized integrated PL intensity extracted from this data is evaluated in Figure 2(c). As P_{RF} increases, the NW emission continuously quenches and is almost completely suppressed for P_{RF} > + 23 dBm. This effect arises from exciton dissociation in the acoustically induced type-II band edge modulation shown schematically in the inset of Figure 2(c). For high P_{RF}, the originally flat bandstructure is superimposed by the piezoelectric potential of the SAW, which separates electrons and holes to stable points in the conduction band (CB) and valence band (VB), respectively. As these points are separated in space by $\lambda_{SAW}/2$, radiative recombination is suppressed.

This simple picture describes well the overall phenomenon of integrated PL suppression. The underlying dynamics of electrons and holes in the acoustically programmed potential require more complete description, advanced spectroscopic techniques, and numerical modeling.[14] We performed phase-locked optical excitation, for which charge carriers are excited at

DOI: 10.1021/acsnano.5b07639
ACS Nano 2016, 10, 4942−4953

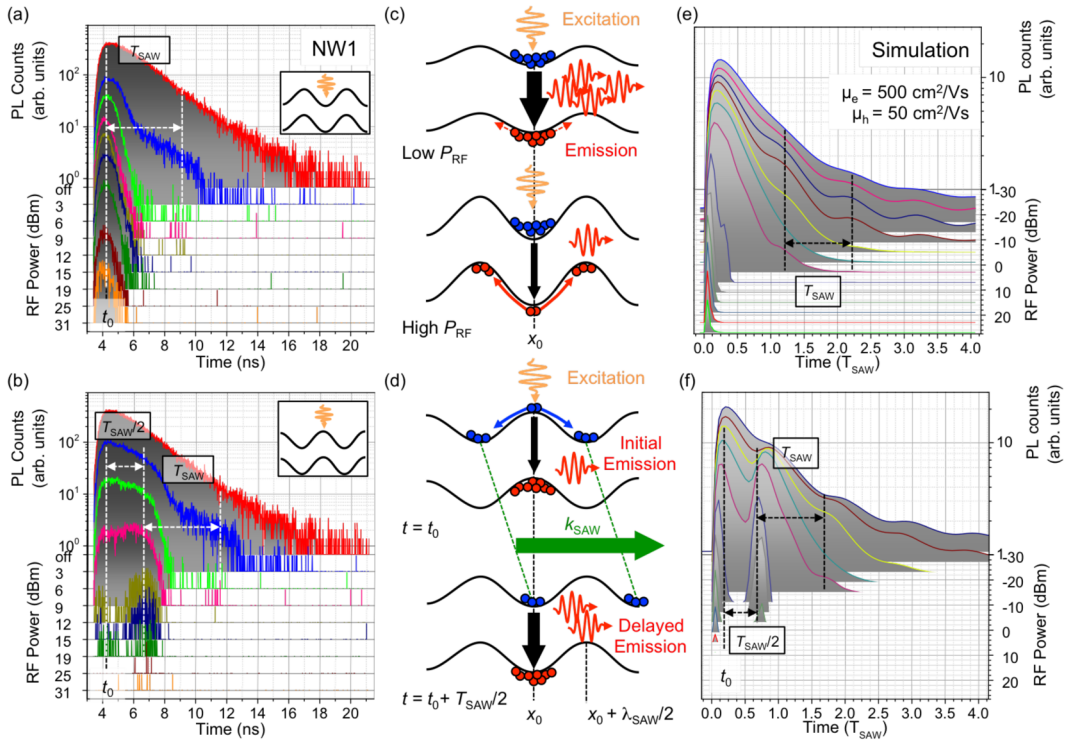

Figure 3. SAW-driven carrier dynamics in a pristine NW. (a,b) Time-resolved PL emission of NW2 for increasing P_{RF} for the phase-locked excitation condition shown in the inset. (c,d) Schematic of the mechanisms underlying the PL modulation observed experimentally in (a,b). (c) For generation of electrons at a stable point in the CB, spatial redistribution of holes becomes more efficient for increasing P_{RF} and responsible of the emission modulation in the experimental data in (a). (d) Electrons generated at an unstable point in the CB efficiently redistribute to stable minima already for moderate P_{RF} while holes remain mostly unaffected by the SAW. Electron transport by the SAW gives rise to the observed $T_{SAW}/2$-delayed emission. (e,f) Calculated PL time-transients for the excitation conditions as in the experimental data shown in (a,b). All characteristics are faithfully reproduced for μ_e = 500 cm^2/(V s) and μ_h = 50 cm^2/(V s). All traces in (a,b,e,f) are offset vertically for clarity.

a precisely defined point during the acoustic cycle (t_0) and recorded the time (t) evolution of the PL of the NW emission (see Methods section). PL time-transients recorded from NW1 for different P_{RF} are presented in Figure 3(a) and (b) for optical generation of electrons and holes at the stable point in the CB and VB, respectively. These different excitation conditions are shown as insets of the two panels. The reference transient of the unperturbed NW emission ($\tau_{PL}^{(NW1)}$ = 1.6 ns) is plotted in red in both panels. As P_{RF} increases the observed transients exhibit clear modulations, which set in for $P_{RF} \geq 0$ dBm, and differ strongly for the two characteristic excitation conditions. For generation of electrons at stable CB minimum (Figure 3(a)), the NW emission is already strongly suppressed for P_{RF} = 3 dBm (blue transient). This suppression indicates that the SAW induced dynamics set in for electrons, which are the carrier species with the higher transport mobility. At this onset, the electron drift velocity (v_{drift}) becomes comparable to the speed of sound. This drift occurs along the NW growth axis and is induced by the SAW's longitudinal electric field component ($\varepsilon_{SAW,L}$). This process becomes the dominant contribution to carrier transport for the drift velocity being comparable or exceeding the speed of sound: $v_{drift} = \mu_e \cdot \varepsilon_{SAW,L} \approx c_s$. For $P_{RF} \geq$ 6 dBm, only a short initial PL burst is detected at the time of photoexcitation as $\mu_e \cdot \varepsilon_{SAW,L} \gg c_s$ and "surfing" carrier transport of electrons sets in. The intensity of this initial PL burst remains approximately constant up to P_{RF} = 12 dBm (brown transient) and decreases monotonically for further increasing P_{RF}. These observations can be understood by taking into account the dynamics of the photogenerated carriers at low and high P_{RF}, illustrated in Figure 3(c). At low $P_{RF} \leq$ 12 dBm, holes are transferred slowly from the point of generation (x_0) to their stable VB maxima (upper panel of Figure 3(c)). At the same time electrons start to move along with the SAW at their stable point in the CB at the speed of sound. Both processes initially lead to a fast and efficient suppression of the NW emission. For $P_{RF} \geq$ 12 dBm, the initially slow hole transfer becomes sufficiently fast to reduce the overlap time with electrons to less than the 300 ps time resolution of our experiment. This fast transfer (lower panel of Figure 3(c)) gives rise to the observed net reduction of the initial PL emission burst and also indicates that $\mu_h \cdot \varepsilon_{SAW,L} \geq c_s$. Thus, for this excitation condition, our time-resolved PL emission monitors the hole transfer process to the stable VB maxima. For the reversed excitation condition, at which electrons are generated at an unstable point, the evolution of the time-transients with increasing P_{RF} exhibits a remarkable difference: in the intermediate power range 6 dBm $\leq P_{RF} \leq$ 15 dBm, the initial PL emission is efficiently quenched, while we clearly detect emission delayed by $\Delta t = T_{SAW}/2$ after photoexcitation. This observation can again be qualitatively explained by taking into account the SAW-induced exciton dissociation and subsequent carrier transport. As illustrated in Figure 3(d), at the time of photoexcitation, electrons are generated at an unstable point in the CB (x_0) at time t. After generation, electrons efficiently transfer to the two adjacent stable points. In contrast, holes remain mostly stationary as their low mobility inhibits transport by the SAW in this power range. After half an acoustic period at time $t + T_{SAW}/2$, the SAW-induced bandstructure modulation

DOI: 10.1021/acsnano.5b07639
ACS Nano 2016, 10, 4942−4953

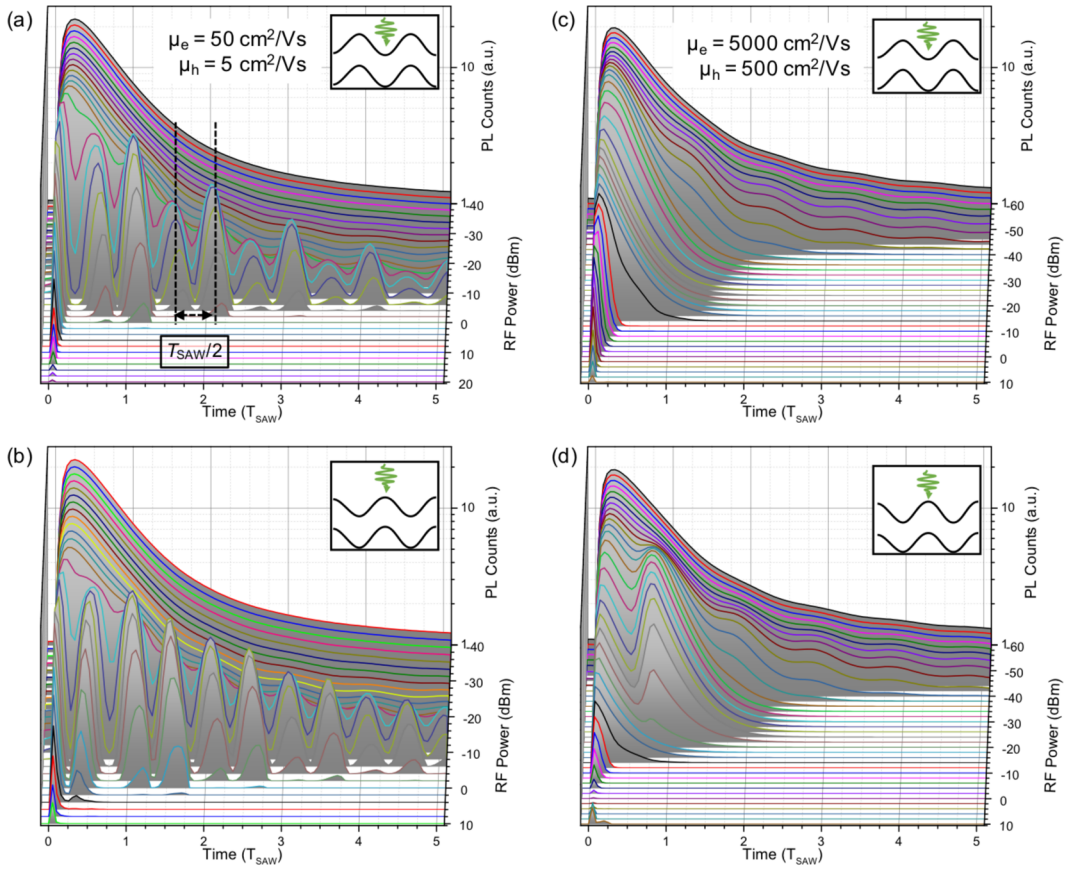

Figure 4. Calculated PL transients for different carrier mobilities. (a,b) Calculated PL time transient for μ_e = 50 cm^2/(V s) and μ_h = 5 cm^2/(V s) for photoexcitation at CB minimum (a) or maximum (b). (c,d) Calculated PL time transient for μ_e = 5000 cm^2/(V s) and μ_h = 500 cm^2/(V s) for photoexcitation at CB minimum (c) or maximum (d). For both sets of mobilities, the calculated transients do not reproduce the experimental data of Figure 3. All traces are offset vertically for clarity.

has translated along the SAW propagation direction (marked by SAW wavevector k_{SAW} in Figure 3(d)) by a $\lambda_{SAW}/2$. Thus, electrons, which initially transferred to the CB minimum located in opposite direction of the SAW propagation (left minimum in Figure 3(d)), are transported back to the point of photoexcitation. Thus, spatial overlap with the stationary holes is re-established, giving rise to the observed re-emergence of the NW emission at $\Delta t = T_{SAW}/2$. The observed temporal characteristics of SAW-modulated PL-emission faithfully follow from a qualitative picture of the induced STCDs.

To support our interpretation and obtain quantitative information on the charge carrier mobilities, we performed numerical calculations of the SAW-induced STCDs and the resulting temporal modulation of the PL emission. Full details on the model can be found in the Methods section and in refs 14, 15, and 43. In Figure 3(e) and (f) we plot calculated time-transients for the two excitation conditions for increasing P_{RF} for a pristine ZB NW. The RF power scale has been calibrated using standard RF characterization data and finite element modeling (see Methods section). Clearly, all characteristic features of the experiment are faithfully reproduced in the simulation data: For both excitation conditions the experimentally observed T_{SAW}-periodic modulations are nicely confirmed. Moreover, the re-emergence of the PL emission at $T_{SAW}/2$ is also well-reproduced for electron generation at an unstable CB-maximum. The two main free parameters in this model are the charge carrier transport mobilities of electrons, μ_e, and holes, μ_h. To obtain excellent agreement between experiment and simulation, we assumed μ_e = 500 cm^2/(V s) and μ_h = 50 cm^2/(V s), respectively. This excellent agreement furthermore underpins, that a few twin boundaries, which are present at low density in the near-pristine NW1, do not significantly impede or even block electron and hole transport. Moreover, electron reflection at longer WZ segments at the end of the NW prevent carrier losses but do not significantly alter the expected PL transients. We note that in our experimental data P_{RF} is weakly but systematically increased compared to values used in our simulations. This is expected due to partial electrostatic screening of $\varepsilon_{SAW,L}$,[44] which leads to an effective reduction of the field and thereby shifts the onset of STCDs to larger P_{RF}.

To obtain faithful values of the carrier mobilites, we varied these and their ratio μ_e:μ_h in our simulations. First, we performed analogous calculations for which we reduced and increased these by 1 order of magnitude. In Figure 4 we plot calculated PL transients for (μ_e = 50 cm^2/(V s) and μ_h = 5 cm^2/(V s)) and (μ_e = 5000 cm^2/(V s) and μ_h = 500 cm^2/(V s)) in panels (a,b) and (c,d). To ensure full comparability with our experimental data, we considered photoexcitation at CB minimum Figure 4(a,c) or CB maximum Figure 4(b,d), respectively. For low mobilities, our calculations predict a $T_{SAW}/2$-periodic modulation of the emission for both excitation conditions. In this regime, $\varepsilon_{SAW,L}$ is not sufficient to induce pronounced hole dynamics for a wide range of P_{RF}. Their low μ_h locks holes to the point of photogeneration. In contrast, weak electron dynamics are induced, and these carriers are

DOI: 10.1021/acsnano.5b07639
ACS Nano 2016, 10, 4942−4953

oscillating back and forth as the SAW propagates. In turn, electrons move across the stationary holes twice per acoustic cycle leading the $T_{SAW}/2$-periodic PL-modulation. This is not observed in our experimental data. For high mobilities, electron and hole dynamics set in already for moderate P_{RF}. Thus, holes are also very efficiently transported away for the point of photogeneration. The most striking consequence is predicted for the characteristic $T_{SAW}/2$-delayed emission for photoexcitation at a CB maximum: in the simulation data in Figure 4(d) this feature is suppressed at lower P_{RF} than the initial PL emission at time $t = 0$. This is in contrast to our experimental data which exhibit exactly the opposite effect. Thus, both increased and reduced mobilities exhibit characteristic deviations from the experimental data. This in turn confirms that the overall range of the transport mobilities for electrons and holes.

Next we vary the ratio of electron and hole mobility which so far was kept constant $\mu_e:\mu_h$ = 10:1. In Figure 5 we investigate the re-emerging PL signal in more detail and plot calculated PL time- transients for constant P_{RF} = 17 dBm and μ_e = 500 cm^2/(V s), but different ratios $\mu_e:\mu_h$. The simulations predict a short initial emission burst due to the fast redistribution of the electrons to the adjacent CB minima (*cf.* Figure 3(d) upper panel). As expected this process only depends on μ_e and is independent of the ratio $\mu_e:\mu_h$. In contrast, the time delayed re-emerging signal increases as μ_h is reduced relative to μ_e because a larger fraction of the holes remains at the point of photogeneration: For $\mu_e:\mu_h$ = 10:1 (black line) the time-delayed emission signal is only weakly resolved, in contrast to our experimental data. However, our simulations nicely predict that the time-delayed signal increases and exceeds the initial emission for $\mu_e:\mu_h$ ranging between 15:1 (blue line) and 25:1 (red line). As our experiments show exactly this characteristic, we can recalibrate $\mu_e:\mu_h$ and conclude that in our NWs μ_h is ~5% of μ_e. We obtain $\mu_e = 500^{+500}_{-250}$ cm^2/(V s), $\mu_h = 50^{+50}_{-30}$ cm^2/(V s) and $\mu_e:\mu_h$ = (20 ± 5):1, values representing the native material limit of vanishing carrier densities for this type of NWs. The stated uncertainties are determined mainly from the RF characterization of the SAW-chip and screening of the SAW's electric fields by the photogenerated carriers. In particular, μ_e = 500 cm^2/(V s) is still more than 2 orders of magnitude lower than the highest reported values exceeding μ_e = 10^5 cm^2/(V s) at 10 K for unintentionally doped GaAs.[45] However, such high mobilities obtained for liquid phase epitaxy-grown bulk material might be out of reach for MBE grown NWs. The less favorable growth conditions will limit the reduction of the defect density. In addition, surface states and sidewall roughness for the high surface-to-volume ratio of NW further increases scattering.

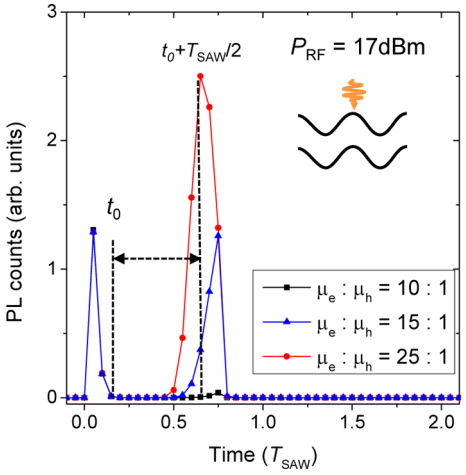

Figure 5. Impact of ratios of $\mu_e:\mu_h$. Calculated PL time-transients for fixed P_{RF} = 17 dBm and μ_e = 500 cm^2/(V s). The intensity of the $T_{SAW}/2$-delayed emission increases for decreasing μ_h pointing toward $\mu_h \approx 0.05\ \mu_e$.

We now turn to NW2, which exhibits a moderate degree of polytypism. In Figure 6(a) we present time-transients of the emission of NW2 recorded for increasing P_{RF}. In this experiment, we employed moderate optical pump intensity and detected the intensity of the dominant ZB emission peak. In strong contrast to NW1, we detect a T_{SAW}-periodic emission, which extends over the entire detection time window. Remarkably, no reduction of this time-delayed signal is

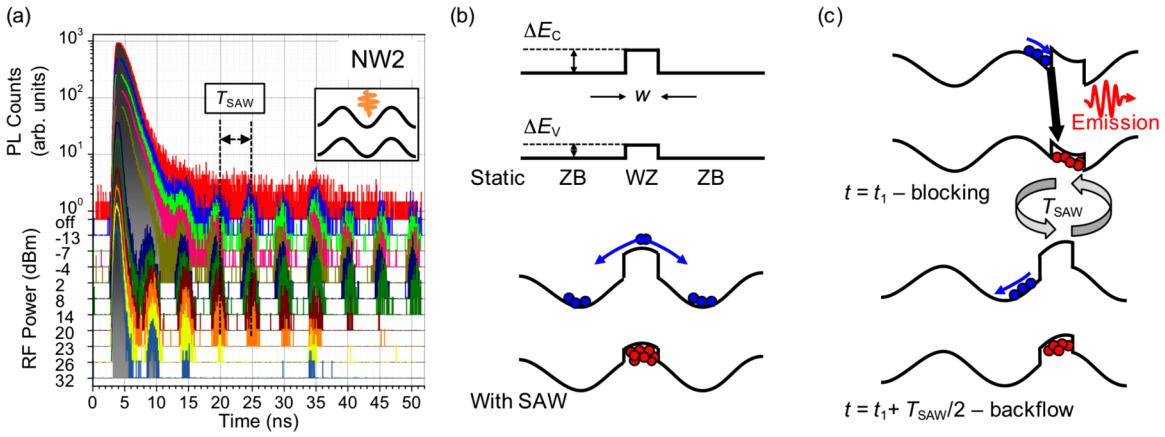

Figure 6. SAW-driven carrier dynamics in a polytypic NW. (a) Time-resolved PL emission of polytypic NW2 for increasing P_{RF} for the phase-locked excitation condition shown in the inset. The transients exhibits a long-time persistent T_{SAW}-periodic "blinking", which is monotonically suppressed as P_{RF} increases. Traces are offset vertically for clarity. (b) Schematic of the band edge modulations of a WZ segment within a ZB NW. A static type-II alignment (upper panel) is superimposed by the SAW-induced piezoelectric potential (lower panel) which enhances exciton dissociation and spatial redistribution. (c) Schematic of the underlying cyclic motion reflection and backflow of electrons: at time t_1 (upper panels) electrons are driven toward the CB barrier and recombine with holes trapped in the WZ segment. At $t_1 + T_{SAW}/2$ (lower panel) electrons flow backward and recombination is suppressed.

DOI: 10.1021/acsnano.5b07639
ACS Nano 2016, 10, 4942–4953

observable for moderate $P_{RF} \leq 14$ dBm during the $t_{det} \approx 50$ ns time window. During that time, the SAW propagates $\Delta x \geq 170$ μm, which is more than 10 times the length of the NW. Thus, we conclude that carriers are effectively retained within the NW and their recombination at the NW ends is suppressed. For $P_{RF} > 14$ dBm, the number of emission bursts within t_{det} decreases and the pulsed time delayed emission is quenched monotonically over a power range of 18 dB (corresponding to a factor of >60).

Similar T_{SAW}-periodic intensity modulation occurring over shorter time scales is weakly resolved in the simulation data presented in Figure 3(e) and (f) for low P_{RF}. It arises from yet ineffective electron transport and almost complete suppression of hole dynamics. This regime can be easily overcome by a slight increase of P_{RF} for pristine NWs. Since pulsed delayed emission is observed over a wide range of P_{RF} for NW2, we conclude that it arises indeed from partially inhibited electron transport and full suppression of hole transport. Both effects can be dramatically enhanced in particular by polytypism. In Figure 6(b) we plot the established type-II band alignment for a WZ-rich segment embedded in a predominantly ZB NW. The SAW-induced potential is again superimposed on this static band structure. As shown schematically in the lower panel of Figure 6(b), the static band structure modulation enhances (i) exciton dissociation, (ii) electron redistribution and (iii) hole localization. The T_{SAW}-periodic intensity modulation can be qualitatively understood by considering the impact of the CB barrier on the SAW-driven electron dynamics. As shown schematically in Figure 6(c), at a given time t_1 during the acoustic cycle, $\varepsilon_{SAW,L}$ drives electrons within the ZB part of the NW toward the CB barrier at the ZB/WZ interface. At this time, radiative recombination with holes trapped in the WZ segment occurs and the corresponding emission is detected. One half period later, at $t_1 + T_{SAW}/2$, $\varepsilon_{SAW,L}$ is reversed and, thus, electrons are efficiently removed from the ZB/WZ interface and the emission is quenched. This full process exhibits the periodicity of the SAW. Moreover, the *static and symmetric* band edge modulation reflects electrons irrespective on the direction of the SAW. This is nicely confirmed in experiments for a forward and backward propagating SAW. As seen in Figure 7, PL-transients recorded for forward (upper panel) and backward propagating SAWs (lower panel), both excited at constant $P_{RF} = 7$ dBm, exhibit practically identical persistent emission modulations. We note that for graded gap potential, similar intensity modulations are expected due to a ratchet effect (tilted washboard potential). However, this effect would only occur for the SAW driving carriers in the direction of a positive gradient.

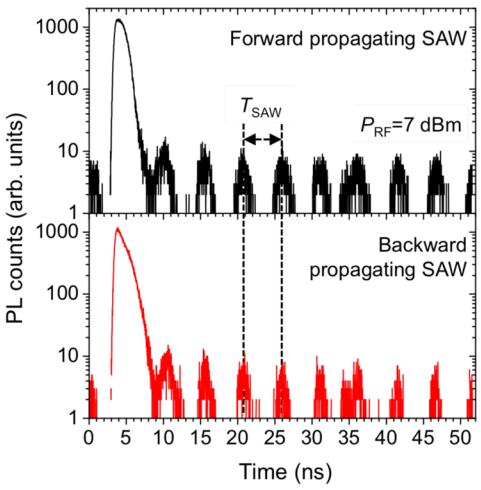

Figure 7. Directionality. Time-resolved emission of polytypic NW2 for a forward (upper panel) and backward (lower panel) propagating SAW.

To fully asses the impact of polytypism, we introduced the static type-II band structure in our simulation: as the simplest model, we assumed a single (w = 500 nm wide) WZ-rich segment in an otherwise pure ZB NW and band offsets were set to ΔE_C = 75 meV and ΔE_V = 55 meV in the CB and VB, respectively. These offsets are conservative upper boundaries derived from values reported in literature.[33,35,36] Again, we used μ_e = 500 cm^2/(V s) and μ_h = 50 cm^2/(V s), which also reproduced the experimental data of NW1. In Figure 8 we summarize calculated electron (blue) and hole (orange) trajectories and the resulting PL transients for different P_{RF} in the lower and upper panels, respectively. Photoexcitation occurs at CB maximum as shown schematically as an inset of Figure 8(a). In both panels time progresses from left to right. In the lower panel the vertical axis is the position along the NW axis which is given in units of the acoustic wavelength. The SAW propagates from top to bottom as indicated by the green arrow. In the upper panel the calculated unperturbed (dashed green) and SAW-modulated PL-transients (solid blue) are each normalized to their respective maximum. For lowest SAW amplitudes (*cf.* Figure 8(a), P_{RF} = −22 dBm) only weak dynamics are induced and no significant PL-modulation is expected. For increasing SAW amplitudes (*cf.* Figure 8(b), P_{RF} = −8 dBm), electron (blue) dynamics are induced by the SAW, while holes (orange) remain fully localized within the WZ segment at x = 0. Indeed, our simulations confirm that electrons in the upper part of the NW are T_{SAW}-periodically pushed toward and removed from the barrier, as shown schematically as an inset. As a direct consequence, the calculated PL transient (blue) clearly exhibits persistent T_{SAW}-periodic emission bursts. For further increasing SAW amplitudes (*cf.* Figure 8(c), P_{RF} = 6 dBm), first electrons can overcome the CB barrier (inset) while hole activation from the WZ segment is weak. In the calculated PL transient, only a single emission burst is expected. At highest SAW amplitudes (*cf.* Figure 8(c), P_{RF} = 28 dBm) electrons easily overcome the CB barrier and holes are removed from the WZ segment (inset). Thus, neither electron reflection nor hole trapping impede the acoustoelectric carrier transport and no time-delayed emission is predicted by these simulations. In Figure 9 we compare in detail such calculated PL-transients as a function of P_{RF}. Clearly, the simulation predicts that T_{SAW}-periodic emission bursts occur over a wide range of P_{RF}. Moreover, the number of bursts monotonically decreases with increasing P_{RF}. Both characteristics are nicely observed in our experimental data shown in Figure 6(a). Again, the P_{RF} scales in the experiment (Figure 6 (a)) and simulation (Figure 9) are offset due to partial screening of $\varepsilon_{SAW,L}$ by photogenerated free carriers.[44]

Finally, we investigate the impact of the CB and VB barrier heights on the T_{SAW}-periodic time delayed emission. In Figure 10, we present simulation results for reduced barriers of ΔE_C = 17.5 meV and ΔE_V = 12.5 meV and P_{RF} = −8 dBm. These data are presented in the same format as that of Figure 8. Clearly, SAW-driven electron dynamics are not efficiently blocked by the barrier between the ZB and WZ regions, as can be seen

DOI: 10.1021/acsnano.5b07639
ACS Nano 2016, 10, 4942−4953

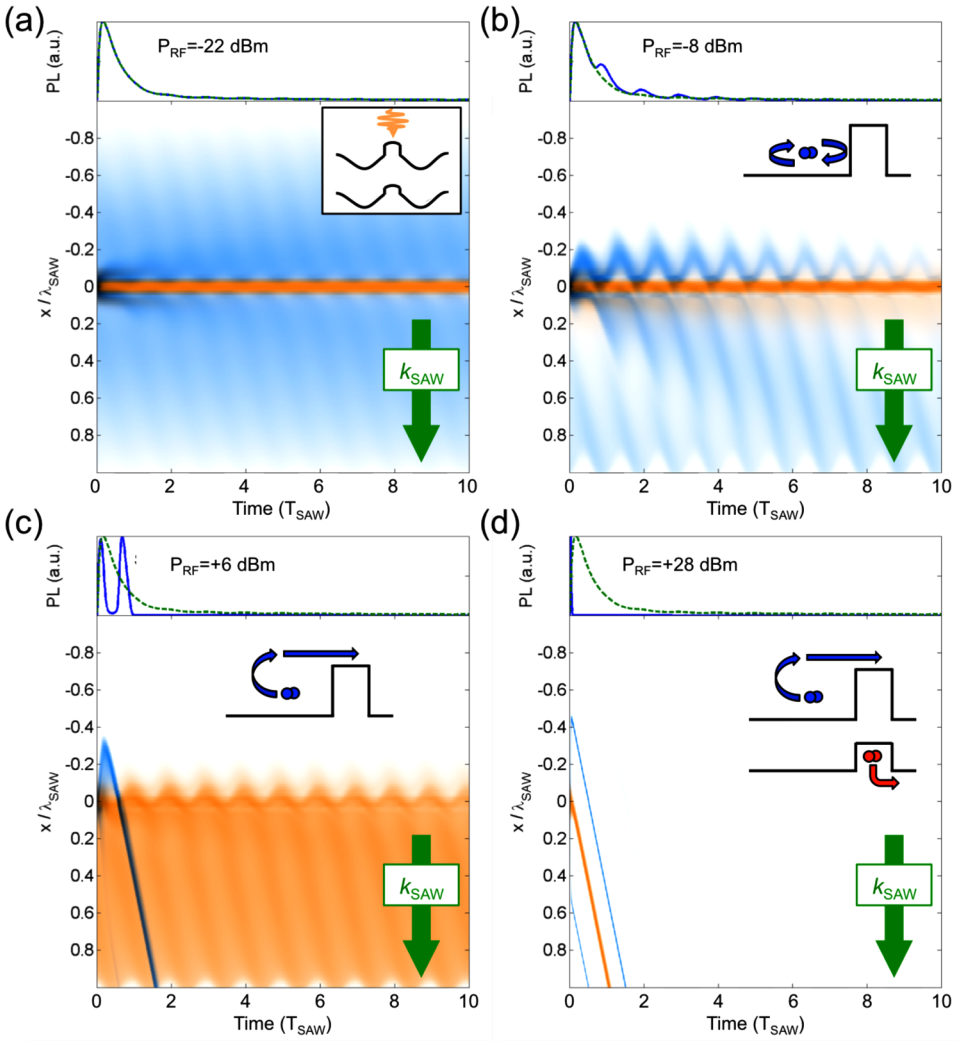

Figure 8. Calculated carrier trajectories and emission dynamics for a polytypic NW. Lower panels: electron (blue) and hole trajectories (orange). The WZ segment is at $x = 0$, the excitation condition is shown as inset of (a). Upper panels: unperturbed (dashed green) and SAW-modulated (blue) PL-transients. For low (a), moderate (b), high (c) and highest (d) SAW-amplitudes. Schematics of respective electron and hole dynamics are included as insets.

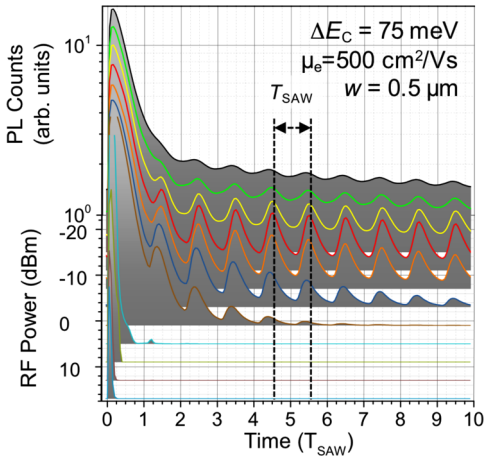

Figure 9. P_{RF}-dependent simulations. Calculated PL transients for increasing P_{RF} for a w = 0.5 μm wide WZ-rich segment and a CB offset of ΔE_C = 75 meV. Calculations nicely reproduce the T_{SAW}-periodic modulation of the NW emission observed in the experiment. Traces are offset vertically for clarity.

from the calculated trajectories in the lower panel. This incomplete blocking is in strong contrast to the data in Figure 8(b) and direct consequence of the reduced barrier height. Moreover, the contrast of T_{SAW}-periodic emission reduces significantly. Since our experimental data shows these emission bursts with high contrast, we can derive $\Delta E_C \approx 20$ meV as a lower boundary for our NWs. We note that length of the WZ segment was assumed to be sufficiently large to readily neglect substantial quantization effects. For shorter segment lengths the effective barriers are reduced by motional quantization. This in turn has no qualitative impact on localization effects.

CONCLUSION

In conclusion, we performed acousto-optoelectric spectroscopy on individual GaAs/AlGaAs core/shell NWs and reproduced the experimentally observed STCDs. By direct comparison of experiment and numerical modeling, we derive the transport mobilities *of both carrier species*, $\mu_e = 500^{+500}_{-250}$ cm^2/(V s), $\mu_h = 50^{+50}_{-30}$ cm^2/(V s) and their ratio μ_e:μ_h = (20 ± 5):1, in the fundamental, native material limit of low carrier density. The obtained mobilities reported here furthermore confirm recent terahertz studies performed at room temperature on ensembles

DOI: 10.1021/acsnano.5b07639
ACS Nano 2016, 10, 4942−4953

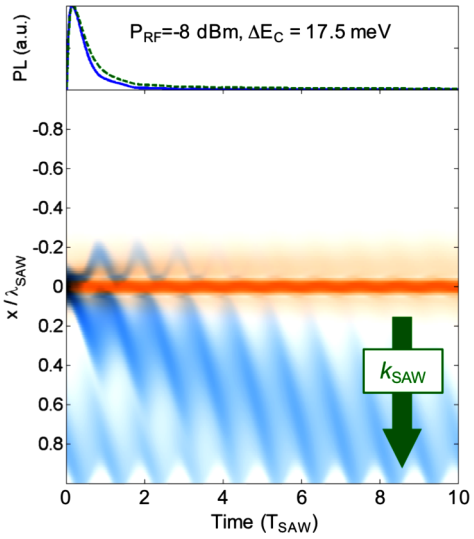

Figure 10. Simulation for reduced barrier height. Calculated electron and hole trajectories (lower panels) and PL time-transient (upper panels) for μ_e = 500 cm^2/(V s) and μ_h = 50 cm^2/(V s). Electrons easily overcome a low barrier in the conduction band in contrast to moderate barrier heights in Figure 8(c).

of similar near-pristine GaAs/AlGaAs core/shell NWs by Parkinson and co-workers,[46] and Joyce and co-workers[47] reporting values approaching the bulk limit. Since the bulk limit is set by scattering with phonons at these temperatures, the results of both studies also point toward a suppression of morphology-related scattering mechanisms, in particular scattering at twin defects. Thelander and co-workers[39] showed in transport experiments pronounced electron scattering of WZ inclusions in contrast to individual twin defects. Our experiments and simulations confirm that even a single longer WZ segment with sufficiently large band offsets efficiently traps holes and acts as a barrier to reflect electrons. Moreover, elaborate local Hall-effect characterization performed by Storm[48] and co-workers and Blömers and co-workers[49] yielded electron mobilities of μ_e = 770 cm^2/(V s) for *n*-doped InP and μ_e = 3600 cm^2/(V s) for InAs NWs, respectively. Finally, we stress that our acousto-optoelectric approach offers several key advantages: in contrast to recently established local Hall-probe techniques, no contacting of NWs is required. Thus, literally any single NW aligned with the SAW propagation can be probed and characterized. This contact-free nature avoids contributions due to Schottky barriers of electrical contacts. Moreover, no doping is required and NWs can be probed in the regime of ultralow carrier concentration at the spatial resolution limit of micro-PL. Acousto-optoelectric spectroscopy can be employed on basically any optically active NW system. For instance it could be performed on InGaAs compounds for telecom applications[50] or to study the impact of QD-like alloy clusters on the electric transport in ternary AlGaAs.[51−53] Our method also enables distinguishing between different optically active quantum confined systems and thus transport channels. For example radial QWs[54,55] can be studied independently on a NW core, which is very challenging using absorption based methods.[56,57] Recently, Fourier-synthesis of arbitrary SAW-waveforms was implemented.[58] This technique enables tailored, nonsinusoidal electric field profiles. In particular, asymmetric waveforms open tantalizing routes toward a more fundamental understanding of STCDs and an improved accuracy for the determination of carrier mobilities.

METHODS

Nanowire Growth. The investigated GaAs/AlGaAs core/shell nanowires are grown by solid-source molecular beam epitaxy in a Ga-assisted autocatalytic growth process on a silicon substrate.[59] Under the selected growth conditions these NWs are expected to be predominantly of zinc blende (ZB) crystal structure with occasional twin defects and have lengths $l_{NW} \geq 10$ μm. However, due to inhomogeneities in substrate temperature and NW density over the as-grown substrate, usually a bimodal distribution of different microstructure is observed in the NWs: predominantly ZB-phase NWs with occasional twin defects, and NWs with intermixed WZ/ZB crystal structure along the NW axis.[37] In radial direction the as-grown NWs consist of a 30−40 nm diameter GaAs core capped by a 24 nm thick $Al_{0.3}Ga_{0.7}As$ shell in order to increase the luminescence efficiency.[60]

SAW-Chip Fabrication and Characterization, and Hybrid Sample Preparation. SAW-chips were fabricated on commercial, oxygen reduced ("black") YZ-cut $LiNbO_{3-x}$ substrates. Delay lines consisting of two IDTs (35 finger pairs, design wavelength λ_{SAW} = 18 μm) were defined by electron beam lithography and finalized in a lift-off process (metallization 10 nm Ti/60 nm Al). A full RF characterization of the IDTs was performed using a vector network analyzer to quantify the mechanical and electrical components of the SAW.[61,62] Using this standard technique, we measured impedances $Z = (46.0 + 9.7j)\Omega$ and $(65.1 + 11.2j)\Omega$ for the IDTs used to excite forward and backward propagating SAWs, respectively. We determined an electric to acoustic power conversion efficiency of 25% for each IDT. This efficiency is constant over the full P_{RF} range in our experiments. The transmission loss of the delay line amounts to 12 dB. The interaction with the NW carrier system was modeled using our recently established finite element modeling (FEM) using Comsol Multiphysics.[24] This method allows to determine $\varepsilon_{SAW,L}$. The uncertainties of these procedures represent the main experimental error of the derived carrier mobilities.

Nanowires were transferred onto the SAW-chip from suspension.[20] Well-isolated individual nanowires aligned with the Z-propagating SAW were identified for later optical experiments using scanning electron microscopy.

Phase-Locked Acousto-optoelectric Spectroscopy. For phase-locked μ-PL, samples are placed in a Helium-flow cryostat equipped with custom-built integrated RF connections and cooled to T = 10 K. An externally triggered diode laser, emitting τ_{laser} = 90 ps long pulses at a wavelength of λ_{laser} = 660 nm, is focused to a d_{laser} = 1.5 μm spot using a ×50 microscope objective. Phase-locked excitation is realized by actively referencing the RF signal exciting the SAW to a clock generator triggering the laser pulse train.[63,64] The laser pulses photoexcite carriers selectively in the core of the NW. The emitted PL is dispersed in a 0.5 m imaging grating monochromator. A liquid N_2-cooled silicon charge coupled device (CCD) is used for time-integrated multichannel acquisition. Full time-resolved experiments are performed using a Si single photon counting module (time resolution ≤300 ps) and time correlation single photon counting (TCSPC) electronics.[43,65] The total time window to record TCSPC histograms is $t_{det} \approx 50$ ns.

Numerical Modeling. In our numerical simulations we calculated the drift and diffusion of electrons and holes in one dimension. Details on the model can be found in refs 14 and 15. The numerical code written in Mathworks Matlab with a graphical user interface and documentation is available free of charge *via* the Internet.[66] The time evolution of the electron (n) and hole (p) densities is given by

$$\frac{\partial n}{\partial t} = D_n \frac{\partial^2 n}{\partial x^2} + \mu_n \frac{\partial(\varepsilon_x \cdot n)}{\partial x} + G(x, t) - R(n \cdot p) \quad (1)$$

$$\frac{\partial p}{\partial t} = D_p \frac{\partial^2 p}{\partial x^2} - \mu_p \frac{\partial(\varepsilon_x \cdot p)}{\partial x} + G(x, t) - R(n \cdot p) \quad (2)$$

DOI: 10.1021/acsnano.5b07639
ACS Nano 2016, 10, 4942−4953

In these equations, G denotes the generation rate. We assume the generation of 10 electron−hole pairs per laser pulse (duration 50 ps) in a 1.5 μm diameter Gaussian spot. R is the exciton recombination rate, derived from the measured PL decay times. The total electric field $\varepsilon_x(x)$ consists of $\varepsilon_{SAW,L}(x)$ and the local electric field induced by the net charge density $p(x) - n(x)$. $\varepsilon_{SAW,L}(x)$ is converted to P_{RF} using the RF characterization described above. Diffusion coefficients at temperature T = 10 K are given by an Einstein relation $D_{n,p} = \mu_{n,p} \cdot \frac{k_B T}{e}$, where e and k_B denote the elementary charge and Boltzmann's constant, respectively. We assume f_{SAW} = 200 MHz, corresponding to λ_{SAW} = 18.56 μm. The length of the NW is $2 \cdot \lambda_{SAW}$ with the excitation spot in the center. For the presented simulations, radiative processes are considered and carriers are nonradiatively lost at the boundary of the simulation region. All calculations were performed over 50 acoustic cycles and four excitation pulses to obtain a stable steady state solution. PL transients are evaluated in the center ±4.4 μm region matched to the optical detection area.

AUTHOR INFORMATION

Corresponding Author

*E-mail: hubert.krenner@physik.uni-augsburg.de.

Notes

The authors declare no competing financial interest.

ACKNOWLEDGMENTS

We gratefully acknowledge support by the Deutsche Forschungsgemeinschaft (DFG) *via* the Nanosystems Initiative Munich (NIM), Sonderforschungsbereich SFB 631 and the Emmy Noether Program (KR3790/2-1), the TUM-IAS Focus group "Nanophotonics", the Marie Curie International Reintegration Grant and the EU-FP7 program SOLID.

REFERENCES

(1) Hoskins, M. J.; Morkoc, H.; Hunsinger, B. J. Charge Transport by Surface Acoustic-Waves in GaAs. *Appl. Phys. Lett.* **1982**, *41*, 332−334.
(2) Wixforth, A.; Kotthaus, J. P.; Weimann, G. Quantum Oscillations in the Surface Acoustic-Wave Attenuation Caused by a Two-Dimensional Electron-System. *Phys. Rev. Lett.* **1986**, *56*, 2104−2106.
(3) Wixforth, A.; Scriba, J.; Wassermeier, M.; Kotthaus, J. P.; Weimann, G.; Schlapp, W. Surface Acoustic-Waves on GaAs $Al_xGa_{1-x}As$ Heterostructures. *Phys. Rev. B: Condens. Matter Mater. Phys.* **1989**, *40*, 7874−7887.
(4) Willett, R. L.; Ruel, R. R.; West, K. W.; Pfeiffer, L. N. Experimental Demonstration of a Fermi Surface at One-half Filling of the Lowest Landau Level. *Phys. Rev. Lett.* **1993**, *71*, 3846−3849.
(5) Shilton, J. M.; Talyanskii, V. I.; Pepper, M.; Ritchie, D. A.; Frost, J. E. F.; Ford, C. J. B.; Smith, C. G.; Jones, G. A. C. High-frequency Single-Electron Transport in a Quasi-One-Dimensional GaAs Channel Induced by Surface Acoustic Waves. *J. Phys.: Condens. Matter* **1996**, *8*, L531−L539.
(6) Rotter, M.; Rocke, C.; Böhm, S.; Lorke, A.; Wixforth, A.; Ruile, W.; Korte, L. Single-Chip Fused Hybrids for Acousto-Electric and Acousto-Optic Applications. *Appl. Phys. Lett.* **1997**, *70*, 2097−2099.
(7) Miseikis, V.; Cunningham, J. E.; Saeed, K.; O'Rorke, R.; Davie, A. G. Acoustically Induced Current Flow in Graphene. *Appl. Phys. Lett.* **2012**, *100*, 133105.
(8) Bandhu, L.; Lawton, L. M.; Nash, G. R. Macroscopic Acoustoelectric Charge Transport in Graphene. *Appl. Phys. Lett.* **2013**, *103*, 133101.
(9) Preciado, E.; Schülein, F. J. R.; Nguyen, A. E.; Barroso, D.; Isarraraz, M.; von Son, G.; Lu, I.-H.; Michailow, W.; Möller, B.; Klee, V.; et al. Scalable Fabrication of a Hybrid Field-Effect and Acousto-Electric Device by Direct Growth of Monolayer MoS_2/$LiNbO_3$. *Nat. Commun.* **2015**, *6*, 8593.
(10) Rocke, C.; Zimmermann, S.; Wixforth, A.; Kotthaus, J. P.; Böhm, G.; Weimann, G. Acoustically Driven Storage of Light in a Quantum Well. *Phys. Rev. Lett.* **1997**, *78*, 4099−4102.
(11) Rocke, C.; Govorov, A. O.; Wixforth, A.; Böhm, G.; Weimann, G. Exciton Ionization in a Quantum Well Studied by Surface Acoustic Waves. *Phys. Rev. B: Condens. Matter Mater. Phys.* **1998**, *57*, R6850−R6853.
(12) Alsina, A.; Santos, P. V.; Hey, R.; García-Cristóbal, A.; Cantarero, A. Dynamic Carrier Distribution in Quantum Wells Modulated by Surface Acoustic Waves. *Phys. Rev. B: Condens. Matter Mater. Phys.* **2001**, *64*, 041304(R).
(13) Santos, P. V.; Alsina, F.; Stotz, J. A. H.; Hey, R.; Eshlaghi, S.; Wieck, A. D. Band Mixing and Ambipolar Transport by Surface Acoustic Waves in GaAs Quantum Wells. *Phys. Rev. B: Condens. Matter Mater. Phys.* **2004**, *69*, 155318.
(14) García-Cristóbal, A.; Cantarero, A.; Alsina, F.; Santos, P. V. Spatiotemporal Carrier Dynamics in Quantum Wells Under Surface Acoustic Waves. *Phys. Rev. B: Condens. Matter Mater. Phys.* **2004**, *69*, 205301.
(15) Schülein, F. J. R.; Pustiowski, J.; Müller, K.; Bichler, M.; Koblmüller, G.; Finley, J. J.; Wixforth, A.; Krenner, H. J. Surface Acoustic Wave Controlled Charge Dynamics in a Thin InGaAs Quantum Well. *JETP Lett.* **2011**, *95*, 575−580.
(16) Wiele, C.; Haake, F.; Rocke, C.; Wixforth, A. Photon Trains and Lasing: The Periodically Pumped Quantum Dot. *Phys. Rev. A: At., Mol., Opt. Phys.* **1998**, *58*, R2680−R2683.
(17) Bödefeld, C.; Ebbecke, J.; Toivonen, J.; Sopanen, M.; Lipsanen, H.; Wixforth, A. Experimental Investigation Towards a Periodically Pumped Single-Photon Source. *Phys. Rev. B: Condens. Matter Mater. Phys.* **2006**, *74*, 035407.
(18) Couto, O. D. D.; Lazić, S.; Iikawa, F.; Stotz, J. A. H.; Jahn, U.; Hey, R.; Santos, P. V. Photon Anti-Bunching in Acoustically Pumped Quantum Dots. *Nat. Photonics* **2009**, *3*, 645−648.
(19) Völk, S.; Knall, F.; Schülein, F. J. R.; Truong, T. A.; Kim, H.; Petroff, P. M.; Wixforth, A.; Krenner, H. J. Surface Acoustic Wave Mediated Carrier Injection into Individual Quantum Post Nano Emitters. *Nanotechnology* **2012**, *23*, 285201.
(20) Kinzel, J. B.; Rudolph, D.; Bichler, M.; Abstreiter, G.; Finley, J. J.; Koblmüller, G.; Wixforth, A.; Krenner, H. J. Directional and Dynamic Modulation of the Optical Emission of an Individual GaAs Nanowire Using Surface Acoustic Waves. *Nano Lett.* **2011**, *11*, 1512−1517.
(21) Hernández-Mínguez, A.; Möller, M.; Breuer, S.; Pfüller, C.; Somaschini, C.; Lazic, S.; Brandt, O.; García-Cristobál, A.; de Lima, M. M.; Cantarero, A.; et al. Acoustically Driven Photon Antibunching in Nanowires. *Nano Lett.* **2012**, *12*, 252−258.
(22) Büyükköse, S.; Hernández-Mínguez, A.; Vratzov, B.; Somaschini, C.; Geelhaar, L.; Riechert, H.; van der Weil, W. G.; Santos, P. V. High-Frequency Acoustic Charge Transport in GaAs Nanowires. *Nanotechnology* **2014**, *25*, 135204.
(23) Weiß, M.; Schülein, F. J. R.; Kinzel, J. B.; Heigl, M.; Rudolph, D.; Bichler, M.; Abstreiter, G.; Finley, J. J.; Wixforth, A.; Koblmüller, G.; et al. Radio Frequency Occupancy State Control of a Single Nanowire Quantum Dot. *J. Phys. D: Appl. Phys.* **2014**, *47*, 394011.
(24) Weiß, M.; Kinzel, J. B.; Schülein; Florian, J. R.; Heigl, M.; Rudolph, D.; Morkötter, S.; Döblinger, M.; Bichler, M.; Abstreiter, G.; Finley, J. J.; et al. Dynamic Acoustic Control of Individual Optically Active Quantum Dot-like Emission Centers in Heterostructure Nanowires. *Nano Lett.* **2014**, *14*, 2256−2264.
(25) Koguchi, M.; Kakibayashi, H.; Yazawa, M.; Hiruma, K.; Katsuyama, T. Crystal Structure Change of GaAs and InAs Whiskers from Zinc-Blende to Wurtzite Type. *Jpn. J. Appl. Phys.* **1992**, *31*, 2061−2065.
(26) Hiruma, K.; Yazawa, M.; Haraguchi, K.; Ogawa, K.; Katsuyama, T.; Koguchi, M.; Kakibayashi, H. GaAs Free-Standing Quantum-Size Wires. *J. Appl. Phys.* **1993**, *74*, 3162.
(27) Ohlsson, B. J.; Björk, M. T.; Magnusson, H. M.; Deppert, K.; Samuelson, L.; Wallenberg, L. R. Size-, Shape-, and Position-

DOI: 10.1021/acsnano.5b07639
ACS Nano 2016, 10, 4942−4953

Controlled GaAs Nano-Whiskers. *Appl. Phys. Lett.* **2001**, *79*, 3335−3337.
(28) Mattila, M.; Hakkarainen, T.; Mulot, M.; Lipsanen, H. Crystal-Structure-Dependent Photoluminescence from InP Nanowires. *Nanotechnology* **2006**, *17*, 1580−1583.
(29) Mattila, M.; Hakkarainen, T.; Jiang, H.; Kauppinen, E. I.; Lipsanen, H. Effect of Substrate Orientation on the Catalyst-Free Growth of InP Nanowires. *Nanotechnology* **2007**, *18*, 155301.
(30) Algra, R. E.; Verheijen, M. A.; Borgstrom, M. T.; Feiner, L.-F.; Immink, G.; van Enckevort, W. J. P.; Vlieg, E.; Bakkers, E. P. A. M. Twinning Superlattices in Indium Phosphide Nanowires. *Nature* **2008**, *456*, 369−372.
(31) Caroff, P.; Dick, K. A.; Johansson, J.; Messing, M. E.; Deppert, K.; Samuelson, L. Controlled Polytypic and Twin-Plane Superlattices in III−V Nanowires. *Nat. Nanotechnol.* **2009**, *4*, 50−55.
(32) Bao, J.; Bell, D. C.; Capasso, F.; Wagner, J. B.; Mårtensson, T.; Trägårdh, J.; Samuelson, L. Optical Properties of Rotationally Twinned InP Nanowire Heterostructures. *Nano Lett.* **2008**, *8*, 836−841.
(33) Spirkoska, D.; Arbiol, J.; Gustafsson, A.; Conesa-Boj, S.; Glas, F.; Zardo, I.; Heigoldt, M.; Gass, M. H.; Bleloch, A. L.; Estrade, S.; et al. Structural and Optical Properties of High Quality Zinc-Blende/Wurtzite GaAs Nanowire Heterostructures. *Phys. Rev. B: Condens. Matter Mater. Phys.* **2009**, *80*, 245325.
(34) Akopian, N.; Patriarche, G.; Liu, L.; Harmand, J.-C.; Zwiller, V. Crystal Phase Quantum Dots. *Nano Lett.* **2010**, *10*, 1098−1102.
(35) Jahn, U.; Lähnemann, J.; Pfüller, C.; Brandt, O.; Breuer, S.; Jenichen, B.; Ramsteiner, M.; Geelhaar, L.; Riechert, H. Luminescence of GaAs Nanowires Consisting of Wurtzite and Zinc-Blende Segments. *Phys. Rev. B: Condens. Matter Mater. Phys.* **2012**, *85*, 045323.
(36) Senichev, A. V.; Talalaev, V. G.; Shtrom, I. V.; Blumtritt, H.; Cirlin, G. E.; Schilling, J.; Lienau, C.; Werner, P. Nanospectroscopic Imaging of Twinning Superlattices in an Individual GaAs-AlGaAs Core−Shell Nanowire. *ACS Photonics* **2014**, *1*, 1099−1106.
(37) Loitsch, B.; Winnerl, J.; Grimaldi, G.; Wierzbowski, J.; Rudolph, D.; Morkötter, S.; Döblinger, M.; Abstreiter, G.; Koblmüller, G.; Finley, J. J. Crystal Phase Quantum Dots in the Ultrathin Core of GaAs−AlGaAs Core−Shell Nanowires. *Nano Lett.* **2015**, *15*, 7544−7551.
(38) Schroer, M. D.; Petta, J. R. Correlating the Nanostructure and Electronic Properties of InAs Nanowires. *Nano Lett.* **2010**, *10*, 1618−1622.
(39) Thelander, C.; Caroff, P.; Plissard, S.; Dey, A. W.; Dick, K. A. Effects of Crystal Phase Mixing on the Electrical Properties of InAs Nanowires. *Nano Lett.* **2011**, *11*, 2424−2429.
(40) Rudolph, D.; Schweickert, L.; Morkötter, S.; Hanschke, L.; Hertenberger, S.; Bichler, M.; Koblmüller, G.; Abstreiter, G.; Finley, J. J. Probing the Trapping and Thermal Activation Dynamics of Excitons at Single Twin Defects in GaAs−AlGaAs Core−Shell Nanowires. *New J. Phys.* **2013**, *15*, 113032.
(41) Demichel, O.; Heiss, M.; Bleuse, J.; Mariette, H.; i Morral, A. F. Impact of Surfaces on the Optical Properties of GaAs Nanowires. *Appl. Phys. Lett.* **2010**, *97*, 201907.
(42) White, R. M.; Voltmer, F. W. Direct Piezoelectric Coupling to Surface Elastic Waves. *Appl. Phys. Lett.* **1965**, *7*, 314−316.
(43) Schülein, F. J. R.; Müller, K.; Bichler, M.; Koblmüller, G.; Finley, J. J.; Wixforth, A.; Krenner, H. J. Acoustically Regulated Carrier Injection into a Single Optically Active Quantum Dot. *Phys. Rev. B: Condens. Matter Mater. Phys.* **2013**, *88*, 085307.
(44) Santos, P. V.; Ramsteiner, M.; Jungnickel, F. Spatially Resolved Photoluminescence in GaAs Surface Acoustic Wave Structures. *Appl. Phys. Lett.* **1998**, *72*, 2099−2101.
(45) Stillman, G. E.; Wolfe, C. M. Electrical Characterization of Epitaxial Layers. *Thin Solid Films* **1976**, *31*, 69−88.
(46) Parkinson, P.; Joyce, H. J.; Gao, Q.; Tan, H. H.; Zhang, X.; Zou, J.; Jagadish, C.; Herz, L. M.; Johnston, M. B. Carrier Lifetime and Mobility Enhancement in Nearly Defect-Free Core−Shell Nanowires Measured Using Time-Resolved Terahertz Spectroscopy. *Nano Lett.* **2009**, *9*, 3349−3353.
(47) Joyce, H. J.; Parkinson, P.; Jiang, N.; Docherty, C. J.; Gao, Q.; Tan, H. H.; Jagadish, C.; Herz, L. M.; Johnston, M. B. Electron Mobilities Approaching Bulk Limits in "Surface-Free" GaAs Nanowires. *Nano Lett.* **2014**, *14*, 5989−5994.
(48) Storm, K.; Halvardsson, F.; Heurlin, M.; Lindgren, D.; Gustafsson, A.; Wu, P. M.; Monemar, B.; Samuelson, L. Spatially Resolved Hall Effect Measurement in a Single Semiconductor Nanowire. *Nat. Nanotechnol.* **2012**, *7*, 718−722.
(49) Blömers, Ch.; Grap, T.; Lepsa, M. I.; Moers, J.; Trellenkamp, S.; Grützmacher, D.; Lüth, H.; Schapers, T. Hall Effect Measurements on InAs Nanowires. *Appl. Phys. Lett.* **2012**, *101*, 152106.
(50) Treu, J.; Stettner, T.; Watzinger, M.; Morkötter, S.; Döblinger, M.; Matich, S.; Saller, K.; Bichler, M.; Abstreiter, G.; Finley, J. J.; et al. Lattice-matched InGaAs-InAlAs Core-Shell Nanowires with Improved Luminescence and Photoresponse Properties. *Nano Lett.* **2015**, *15*, 3533−3540.
(51) Mancini, L.; Fontana, Y.; Conesa-Boj, S.; Blum, I.; Vurpillot, F.; Francaviglia, L.; Russo-Averchi, E.; Heiss, M.; Arbiol, J.; Morral, A. F. i.; et al. Three-Dimensional Nanoscale Study of Al Segregation and Quantum Dot Formation in GaAs/AlGaAs Core-Shell Nanowires. *Appl. Phys. Lett.* **2014**, *105*, 243106.
(52) Jeon, N.; Loitsch, B.; Morkoetter, S.; Abstreiter, G.; Finley, J.; Krenner, H. J.; Koblmueller, G.; Lauhon, L. J. Alloy Fluctuations Act as Quantum Dot-like Emitters in GaAs-AlGaAs Core−Shell Nanowires. *ACS Nano* **2015**, *9*, 8335−8343.
(53) Lazić, S.; Chernysheva, E.; Gačević, Ž.; van der Meulen, H. P.; Calleja, E.; Calleja Pardo, J. M. Dynamic Control of the Optical Emission from GaN/InGaN Nanowire Quantum Dots by Surface Acoustic Waves. *AIP Adv.* **2015**, *5*, 097217.
(54) Fickenscher, M.; Shi, T.; Jackson, H. E.; Smith, L. M.; Yarrison-Rice, J. M.; Zheng, C.; Miller, P.; Etheridge, J.; Wong, B. M.; Gao, Q.; et al. Optical, Structural, and Numerical Investigations of GaAs/AlGaAs Core−Multishell Nanowire Quantum Well Tubes. *Nano Lett.* **2013**, *13*, 1016−1022.
(55) Fontcuberta i Morral, A.; Spirkoska, D.; Arbiol, J.; Heigoldt, M.; Morante, J. R.; Abstreiter, G. Prismatic Quantum Heterostructures Synthesized on Molecular-Beam Epitaxy GaAs Nanowires. *Small* **2008**, *7*, 899−903.
(56) Erhard, N.; Zenger, S.; Morkötter, S.; Rudolph, D.; Weiss, M.; Krenner, H. J.; Karl, H.; Abstreiter, G.; Finley, J. J.; Koblmüller, G.; et al. Ultrafast Photodetection in the Quantum Wells of Single AlGaAs/GaAs-Based Nanowires. *Nano Lett.* **2015**, *15*, 6869−6874.
(57) Badada, B. H.; Shi, T.; Jackson, H. E.; Smith, L. M.; Zheng, C.; Etheridge, J.; Gao, Q.; Tan, H. H.; Jagadish, C. Quantum Confined Stark Effect in a GaAs/AlGaAs Nanowire Quantum Well Tube Device: Probing Exciton Localization. *Nano Lett.* **2015**, *15*, 7847−7852.
(58) Schülein, F. J. R.; Zallo, E.; Atkinson, P.; Schmidt, O. G.; Trotta, R.; Rastelli, A.; Wixforth, A.; Krenner, H. J. Fourier Synthesis of Radiofrequency Nanomechanical Pulses with Different Shapes. *Nat. Nanotechnol.* **2015**, *10*, 512−516.
(59) Rudolph, D.; Hertenberger, S.; Bolte, S.; Paosangthong, W.; Spirkoska, D.; Döblinger, M.; Bichler, M.; Finley, J. J.; Abstreiter, G.; Koblmüller, G. Direct Observation of a Noncatalytic Growth Regime for GaAs Nanowires. *Nano Lett.* **2011**, *11*, 3848−3854.
(60) Rudolph, D.; Funk, S.; Döblinger, M.; Morkötter, S.; Hertenberger, S.; Schweickert, L.; Becker, J.; Matich, S.; Bichler, M.; Spirkoska, D.; et al. Spontaneous Alloy Composition Ordering in GaAs-AlGaAs Core−Shell Nanowires. *Nano Lett.* **2013**, *13*, 1522−1527.
(61) Datta, S. *Surface Acoustic Wave Devices*; Prentice Hall: Englewood Cliffs, NJ, 1986.
(62) Morgan, D. *Surface Acoustic Wave Filters*; Academic Press: Amsterdam, 2007.
(63) Völk, S.; Knall, F.; Schülein, F. J. R.; Truong, T. A.; Kim, H.; Petroff, P. M.; Wixforth, A.; Krenner, H. J. Direct Observation of Dynamic Surface Acoustic Wave Controlled Carrier Injection into Single Quantum Posts Using Phase-Resolved Optical Spectroscopy. *Appl. Phys. Lett.* **2011**, *98*, 023109.

DOI: 10.1021/acsnano.5b07639
ACS Nano 2016, 10, 4942−4953

(64) Fuhrmann, D. A.; Thon, S. M.; Kim, H.; Bouwmeester, D.; Petroff, P. M.; Wixforth, A.; Krenner, H. J. Dynamic Modulation of Photonic Crystal Nanocavities Using Gigahertz Acoustic Phonons. *Nat. Photonics* **2011**, *5*, 605−609.
(65) Kapfinger, S.; Reichert, T.; Lichtmannecker, S.; Müller, K.; Finley, J. J.; Wixforth, A.; Kaniber, M.; Krenner, H. J. Dynamic Acousto-Optic Control of a Strongly Coupled Photonic Molecule. *Nat. Commun.* **2015**, *6*, 8540.
(66) Schülein, F. J. R. *chargeDynamics—Simulation code for Mathworks Matlab with Graphical User Interface*; http://www.nanoquakes.de/chargeDynamics (accessed March 18th 2016).

DOI: 10.1021/acsnano.5b07639
ACS Nano 2016, 10, 4942−4953